

## WIND STRUCTURE OF THE WOLF-RAYET STAR EZ CMA=HD 50896

Aaron Flores,<sup>1</sup> Gloria Koenigsberger,<sup>2</sup> Octavio Cardona,<sup>3</sup> and Lelio de la Cruz<sup>1</sup>

Received 2011 March 22; accepted 2011 May 9

### RESUMEN

Presentamos los resultados del análisis de la línea de N V 4604 observada en espectros de la estrella Wolf-Rayet HD 50896 obtenidos en 1991, 1999, 2005 y 2009. Mostramos que la variabilidad de esta línea es consistente con un modelo en el que la opacidad del viento sufre cambios cíclicos con un periodo de 3.76 d o bien con un modelo de un viento con estructura cuadrupolar donde cada sector tiene una opacidad distinta.

### ABSTRACT

The Wolf-Rayet star HD 50896 (EZ CMa=WR6) is well-known for the emission-line profile variability that occurs on a 3.7-day timescale. In particular, the shape of the N V 4604-21 doublet changes from a P Cygni profile to one in which no blue-shifted absorption component is present. In this paper we use spectroscopic observations obtained in 1991, 1999, 2005 and 2009 to glean physical conditions within the stellar wind that may give rise to these changes. We find that variations in the opacity at a distance  $r/R_{\max} \sim 0.3-0.5$  of the stellar surface can produce the observed effects. Here,  $R_{\max}$  is the extent of the N V line-forming region. The results are consistent either with a scenario in which the opacity of the inner wind region of HD 50896 undergoes cyclical variations over the 3.76 d period or with a quadrupolar wind distribution in which the sectors having different opacities rotate in and out of our line-of-sight on this periodic timescale.

*Key Words:* stars: individual (EZ CMa = HD 50896) — stars: winds, outflows — stars: Wolf-Rayet

### 1. INTRODUCTION

Classical Wolf-Rayet (WR) stars (van der Hucht et al. 1981) are the evolved remnants of massive O-type stars and are believed to be the last stable evolutionary phase of a star before it explodes as a supernova or, possibly, a “collapsar” (Crowther 2007). The WR stars are often found in binary systems in which the companion is also a massive O-type star. Van den Heuvel (1976) noted that after the more massive star in a massive binary system has become a supernova, leaving a neutron star or black hole remnant, its companion should eventually become a WR star. Hence, a number of *WR+cc* systems should be observable at any given time. The WN5-

type star HD 50896 (EZ CMa=WR6; van der Hucht et al. 1981) was the first WR star to be proposed to fit this evolutionary scenario. Firmani et al. (1979, 1980) detected periodic ( $P = 3.76$  d) emission-line profile variability which, when combined with the fact that HD 50896 is surrounded by a ring nebula (S308) and that it lies high above the galactic plane<sup>4</sup>, led them to conclude that HD 50896 is a binary system with a low-mass companion. Shortly thereafter, linear polarization (McLean 1980) and photometric (Cherepashchuk 1981) observations confirmed the  $P = 3.76$  day periodicity. Subsequent period determinations by Lamontagne, Moffat, & Lamarre (1986) and Georgiev et al. (1999) gave, respectively  $P = 3.766 \pm 0.001$  d and  $P = 3.765 \pm 0.001$  d.

Two criteria were used by Firmani et al. (1979, 1980) to determine the original period: (a) the shape of the He II 4686 line profiles, particularly the lo-

<sup>1</sup>Facultad de Ingeniería, Universidad Autónoma del Carmen, Campeche, Mexico.

<sup>2</sup>Instituto de Ciencias Físicas, Universidad Nacional Autónoma de México, Mexico.

<sup>3</sup>Instituto Nacional de Astrofísica Óptica y Electrónica, Puebla, Mexico.

<sup>4</sup>Suggesting it is a “runaway” system as a consequence of the supernova “kick”.

cation of superposed emission-like spikes that were either at line center, or “blueward”, or “redward” of this location; and (b) the strength of the N V 4604-21 P Cygni absorptions. Georgiev et al. (1999) showed that the variations in this high ionization N V doublet retained coherence over  $\sim 14$  years of observations, with a period  $P = 3.765$  d. However, although the variability in other lines and in photometric data is always consistent with the 3.76 d period, it is often not coherent over timescales of several weeks or longer (Drissen et al. 1989). Hence, the binary nature of HD 50896 has been questioned.

Another problem with the *WR+cc* scenario for HD 50896 is the absence of significant X-ray variability. Stevens & Willis (1988) and Skinner, Itoh, & Nagase (1998) showed that the observed levels of X-ray emission were far too low to be attributable to accretion onto a neutron star or black hole. On the other hand, Skinner et al. (2002) concluded that the presence of a low-mass companion upon which the WR wind collides would be consistent with the low X-ray emission levels. Hence, the binary scenario is still a viable one. However, even under the binary hypothesis, a physical mechanism by which the line-profile variability occurs is still not identified.

In this investigation we focus on one of the physical mechanisms that may produce the observed line-profile variations in HD 50896. Specifically, we will analyze the N V 4604 line profiles in order to determine the type of wind structure variations that may produce the observed variability. In § 2 we describe the observations; § 3 contains a description of the N V variability; § 4 describes the line-fitting technique; § 5 contains a discussion; and § 6 the conclusions.

## 2. OBSERVATIONS

The new observations were carried out during three epochs in 1999, 2005 and 2009 (hereafter referred to as OGH I, OGH II and OGH III, respectively), with the 2.1 m telescope of the Observatorio Astronómico Guillermo Haro (OGH), using a Boller & Chivens spectrograph, with a 830 grooves  $\text{mm}^{-1}$  grating in the second order, and a slit aperture of 250  $\mu\text{m}$ . A Schott BG18 blocking filter was placed at the slit entrance, thus removing light at  $\lambda < 4000$  Å. For the first and second epochs, we used a CCD with a  $1024 \times 1024$  Tek chip and for the third epoch a CCD with  $1300 \times 1300$  BestArray chip. The reciprocal dispersion for the first and second epochs was 0.31 Å/pix, and the spectral window was  $\lambda\lambda 4463\text{--}4778$  Å, while for the third epoch, the corresponding parameters were 0.26 Å/pix, and  $\lambda\lambda 4470\text{--}4810$  Å.

Data reduction was performed using standard procedures in the Image Reduction and Analysis Facility (IRAF) version 2.14.1 package<sup>5</sup>, which included bias subtraction, flat field correction, cosmic ray deletion, and wavelength calibration. The wavelength calibration was performed using a He-Ar comparison lamp, yielding an uncertainty of 0.34 Å in wavelength measurements for the OGH II and OGH III epochs. For the OGH I epoch, due to a problem with the comparison lamp spectrum, the wavelength calibration was deficient, leading to uncertainties twice as large. Individual spectra have  $S/N \sim 110$  at the continuum level, with the average spectra per night having  $S/N \sim \sqrt{n}110$ , where  $n = 3, \dots, 35$  is the number of spectra averaged. The individual spectra were normalized to the continuum level after interpolating a third-order Legendre polynomial function to line-free spectral regions.

One of the noteworthy features of these observations is the fact that each set was obtained over seven or eight consecutive nights, thus covering two contiguous 3.76-day cycles. On each night, between 3 and 35 spectra were obtained within time intervals ranging from one to six hours. The three sets of data are comprised of 151 spectra. Table 1 contains the journal of observations. Column 1 lists the identification number of the spectrum, Column 2 the mean Julian Date  $-2445000$ , Column 3 the date of observations, Column 4 the number of spectra obtained over the night, Column 5 the timespan (in hours) over which these spectra were collected and Column 6 the phase computed with  $P = 3.7650$  d and  $T_0 = 2443199.53$  from Georgiev et al. (1999).

The above data sets were complemented with a set of nightly average spectra obtained in the Observatorio Astronómico Nacional San Pedro Mártir (SPM) during 1991 January (Piceno 2003; Vázquez 2003; Morel et al. 1998; Georgiev et al. 1999). The date of observation, number of spectra averaged, and nightly timespan covered by these spectra are listed in Table 2. The SPM data set covers 13 consecutive nights. Only one spectrum was obtained on nights “a” and “d” due to bad weather; the first of these is a useful spectrum having  $S/N \sim 100$ . On night “d” the spectrum has  $S/N \sim 35$  and was not used for the analysis presented in this paper. This set provides spectra for three consecutive cycles in the 3.76 d period.

<sup>5</sup>IRAF is distributed by the National Optical Astronomy Observatory, which is operated by the Association of Universities for Research in Astronomy, Inc., under cooperative agreement with the National Science Foundation.

TABLE 1

JOURNAL OF OBSERVATIONS FOR THE OGH SPECTRA AND LINE FIT PARAMETERS<sup>a</sup>

ID	JD	Day	n	$\Delta t$	$\phi$	$V_{\max}$	$X_0$	$X_1$	$R_1$	$X_2$	$R_2$	$X_3$	$R_3$	$X_4$	Type
<b>OGH I (Jan-Feb 1999)</b>															
b24	1202.80	24	9	1.0	0.71	40	0.1	90	1.25	380	1.90	210	3.1	10.	a
b25	1203.73	25	35	6.0	0.96	34	0.1	40	1.38	370	2.10	160	2.9	10.	a
b26	1204.82	26	3	0.5	0.25	34	0.1	45	1.25	320	2.00	180	2.6	10.	a
b27	1205.71	27	25	5.0	0.48	40	0.1	45	1.45	710	2.00	60	2.7	0.1	s
b28	1206.76	28	15	2.0	0.76	34	0.1	50	1.25	310	1.90	220	2.4	70	a
b30	1208.70	30	19	2.7	0.28	38	0.1	40	1.30	410	1.88	180	2.95	60	a
b31	1209.70	31	10	2.0	0.54	42	0.1	45	1.30	640	1.90	40	2.7	0.1	s
b2	1211.70	02	35	6.0	0.07	38	0.1	46	1.40	500	2.00	70	3.0	0.1	w
<b>OGH II ( Nov 2005)</b>															
n19	3693.84	19	8	1.0	0.37	34	20.	50	1.35	320	1.9	140	3.1	50.	a
n20	3694.96	20	10	2.7	0.64	36	0.1	55	1.30	360	1.95	75	2.7	0.1	w
n21	3695.97	21	15	2.2	0.91	35	20.	50	1.25	370	1.85	110	3.1	50.	a
n22	3696.98	22	20	5.0	0.17	40	0.1	45	1.40	650	1.85	20	2.7	0.1	s
n23	3697.96	23	7	1.0	0.44	35	0.1	50	1.25	270	1.70	140	3.8	50	a
n24	3698.95	24	5	1.0	0.70	33	0.1	60	1.35	340	1.95	33	2.9	80	w
n25	3699.98	25	10	2.7	0.97	33	0.1	40	1.40	400	2.20	93	2.9	0.8	w
n26	3700.87	26	20	5.0	0.21	40	0.1	45	1.40	700	1.85	8	2.7	0.1	s
<b>OGH III (Feb 2009)</b>															
d02	4864.82	02	15	1.0	0.36	33	0.1	60	1.46	400	2.05	73	2.9	0.1	w
d03	4865.74	03	20	2.7	0.60	38	0.1	43	1.40	520	2.00	40	2.7	0.1	s
d04	4866.77	04	14	2.2	0.88	34	0.1	60	1.30	280	1.90	140	2.8	40	a
d05	4867.75	05	22	5.0	0.14	38	10.	60	1.40	420	1.80	90	2.8	1	w
d06	4868.77	06	20	1.0	0.41	36	10.	60	1.39	400	2.0	60	3.0	0.1	w
d07	4869.78	07	15	1.0	0.68	35	0.1	45	1.40	400	2.00	45	2.7	0.1	s
d08	4870.71	08	6	2.7	0.92	34	0.1	60	1.38	250	1.80	110	3.0	60	a

<sup>a</sup>Mean Julian dates ( $-2450000$ ) for the time interval ( $\Delta t$ ) over which the data  $n$  spectra were collected. Phase ( $\phi$ ) is computed with the Georgiev et al. (1999) ephemeris. The fit parameters are described in the text. For all cases,  $R_{\max} = 4.2 R_*$ ,  $R_a = 3.9 R_*$  and  $V_{\text{th}} = 50 \text{ km s}^{-1}$ .

TABLE 2

JOURNAL OF OBSERVATIONS FOR THE SPM SPECTRA AND LINE FIT PARAMETERS<sup>a</sup>

ID	JD	n	$\Delta t$	Phase	$V_{\max}$	$X_0$	$X_1$	$R_1$	$X_2$	$R_2$	$X_3$	$R_3$	$X_4$	Type
a	280.9	1	–	0.63	36	0.1	47	1.21	410	2.02	30	2.9	0.1	s
b	281.8	22	4.5	0.87	37	0.1	59	1.40	510	2.05	18	3.0	0.1	s
c	282.8	34	6.1	0.14	34	0.1	90	1.40	250	1.95	130	3.2	9	a
e	284.8	30	5.7	0.67	31	0.1	10	1.20	330	2.2	58	2.9	1	w
f	285.8	22	5.1	0.93	37	0.1	67	1.36	460	2.02	20	2.8	0.1	s
g	286.8	32	4.9	0.20	34	0.1	90	1.27	220	1.85	130	3.2	9	a
h	287.8	35	4.5	0.47	31	0.1	30	1.30	290	2.1	78	2.9	1	w
i	288.7	7	0.6	0.70	31	0.1	30	1.40	340	2.2	58	3.0	1	w
j	289.8	34	5.5	0.00	35	20	51	1.35	390	2.12	37	2.8	0.1	s
k	290.7	7	3.4	0.24	34	0.1	90	1.35	260	1.7	120	3.5	9	a
l	291.8	40	4.4	0.53	31	0.1	30	1.40	340	2.24	60	3.0	1	w

<sup>a</sup>Mean JD's are  $-2448000$ . Other parameters as in Table 1.

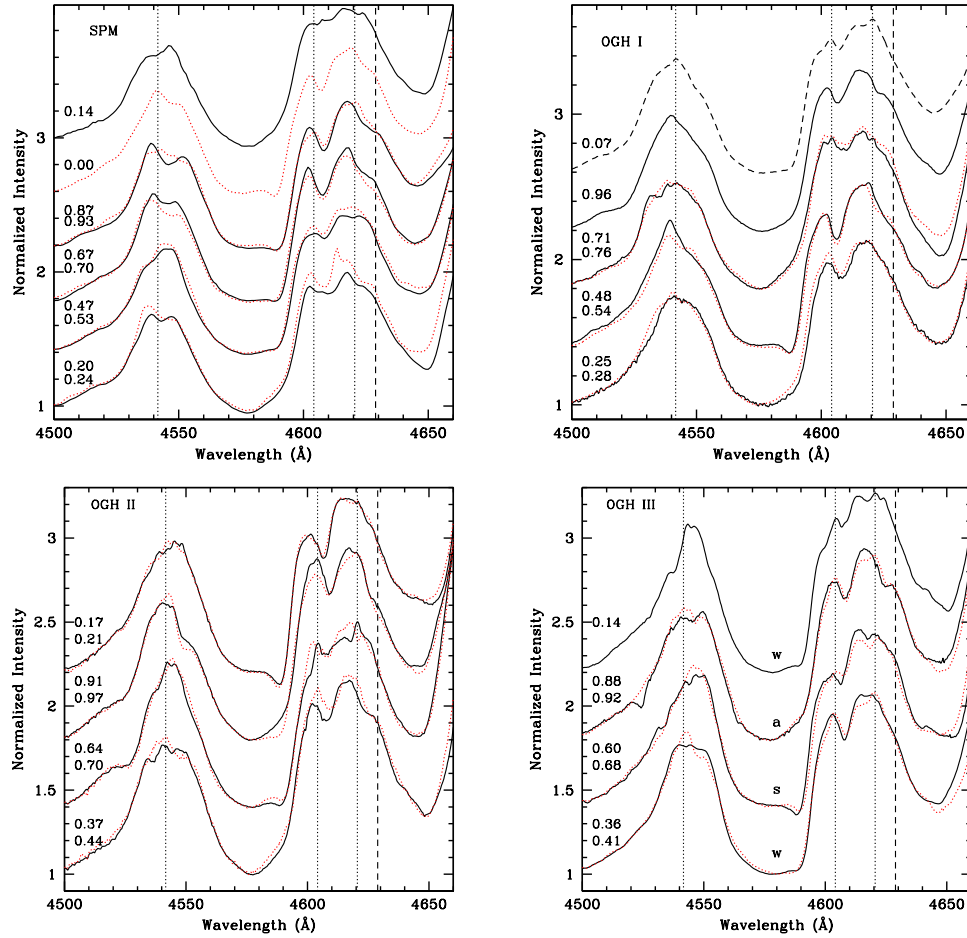


Fig. 1. Spectra from 1991 (SPM; top left), 1999 (OGH I; top right), 2005 (OGH II; bottom left) and 2009 (OGH III; bottom right). Spectra from the first 3.76 d cycle are shown with a continuous line, those from the second cycle are shown with dots, with spectra of similar orbital phases having the same vertical shift in the plot. Orbital phases with the Georgiev et al. (1999) ephemeris are listed. Vertical dotted lines indicate laboratory wavelengths of He II 4541.59, N V 4604.14 and N V 4620.50; the dashed line marks the location of O V 4628.87, a possible contributor to the blend. The letters *s*, *w* and *a* in the OGH III panel label the type of P Cygni absorption (see text). The color figure can be viewed online.

### 3. N V LINE-PROFILE VARIABILITY

Figure 1 shows the spectral region containing the He II 4542 and the N V 4604-21 doublet for the four epochs of observations. Spectra are displaced vertically to allow a clear view of their characteristics at different phases. Given that the observations of all four epochs were carried out over at least two 3.765 d cycles, two spectra per epoch at similar phases are generally available. The spectrum from the second cycle is plotted with dots. Phases were computed using the Georgiev et al. (1999) ephemeris and are listed.

The variations in the N V 4604-21 doublet can be described primarily in terms of the occasional presence of a prominent P Cygni absorption component

which at other times is absent, and an intermediate state in which the absorption is weak. Although the same type of variability is present in all epochs, a comparison of the four panels in Figure 1 leads to the conclusion that a particular profile shape does not always appear in the same 3.76 d phase interval. For example, the P Cygni absorption component is strong at  $\phi \sim 0.9 - 1.0$  in the SPM data, at  $\phi \sim 0.5$  in the OGH I data; at  $\phi \sim 0.2$  in the OGH II data, and  $\phi \sim 0.6 - 0.7$  in the OGH III spectra. Hence, the presence of a strong P Cygni absorption does not correlate with phase for spectra separated in time by a few years, as are our data. However, on timescales of less than a couple of weeks, a phase-dependence does exist.

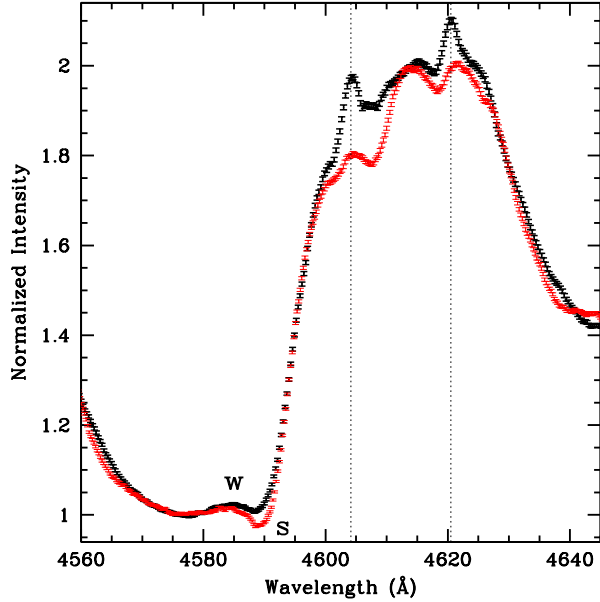


Fig. 2. Comparison between spectrum n20 and spectrum d07 illustrating the difference between the *weak* (w; black) and *strong* (s; red) types of absorption in N V 4604. Error bars indicate the uncertainties associated with each spectrum, as determined from the corresponding S/N ratios. The color figure can be viewed online.

TABLE 3

DAY-TO-DAY P CYGNI TYPE FOR EACH EPOCH<sup>a</sup>

Epoch	Type											
1991	s	s	a	-	w	s	a	w	w	s	a	w
1999	-	-	a	a	a	s	a	-	a	s	-	w
2005	-	-	a	w	a	s	a	w	w	s	-	-
2009	-	-	-	-	w	s	a	w	w	s	a	-

<sup>a</sup>Each entry of the table corresponds to one night of observations, and they are listed sequentially starting at the left with the first night of data. The letters indicate whether the N V 4604 profile has a *strong*, *weak* or *absent* P Cygni absorption component. The nights of each epoch have been aligned so that the *s* spectra all lie along the same columns. A dash indicates no data available for the given night.

We assign a classification of *strong*, *weak*, or *absent* to the type of line-profile observed. The distinction between the three types of profiles is most clearly seen at  $\lambda$  4590 Å in Figure 1. The *weak* profiles have intensities that are very close to the continuum level, the *strong* profiles are below the contin-

uum, and the *absent* profiles lie significantly above it. The continuum level lies at intensity level unity, by definition from the spectrum normalization process. Examples of the *strong* and the *weak* type profiles are shown in Figure 2. In Tables 1 and 2 each spectrum has been characterized with the letters *s*, *w* or *a* in accordance with this classification. Using this description for the N V profiles, the day-to-day variability pattern of the four epochs may be compared. Table 3 illustrates this variability pattern for each epoch individually (the different rows) and for the entire set by aligning the first *s* spectrum of the OGH data sets with the second *s* of the SPM set in the same column. Table 3 shows that the four epochs follow the same sequence that repeats with the 3.76 d period:  $s \rightarrow a \rightarrow w/a \rightarrow a/w$ , where *a/w* and *w/a* indicate that either *a* or *w* are present in the column.

Figure 1 also shows that part of the variability is due to the appearance of narrow emission peaks. A clear example of such features at the rest wavelength of He II 4642, N V 4604 and N V 4621 can be seen in the phase interval 0.64–0.70 of the OGH II spectra (see also Figure 2). Thus, in addition to the changing P Cyg absorption, the line-profile variability involves the presence of narrow, superposed emissions. The fact that they are located at the laboratory wavelength indicates that they originate in material that is flowing perpendicular to our line-of-sight.

Figure 3 again shows the spectral region containing He II 4542 and the N V 4604–21 doublet for the four epochs of observations. In this case, the first spectrum plotted from bottom to top is the first spectrum in the series having a *strong* N V 4604 P Cygni absorption component. In the SPM data set, we chose spectrum ‘b’ of the series because on night ‘a’ only 1 spectrum was obtained<sup>6</sup>. The second spectrum from bottom up, plotted with a +0.5 shift in the intensity scale, is the one obtained during the following night of observation; the third and fourth spectra correspond to the subsequent 2 nights, each with a corresponding additional +0.5 shift in the intensity scale. The fifth spectrum of the series is overlaid with the first, this time with a dotted line instead of a continuous line; similarly, with the following spectra of the series. This figure confirms the similarity between the four epochs’ N V line profile variability, but it also shows that small changes in the line shapes are present for spectra of similar phases separated by a single 3.76 d cycle. The magnitude of these small changes may be evaluated from the ratios

<sup>6</sup>We do note, however, that spectrum ‘a’ has an *s*-type profile which apparently breaks the pattern described above.

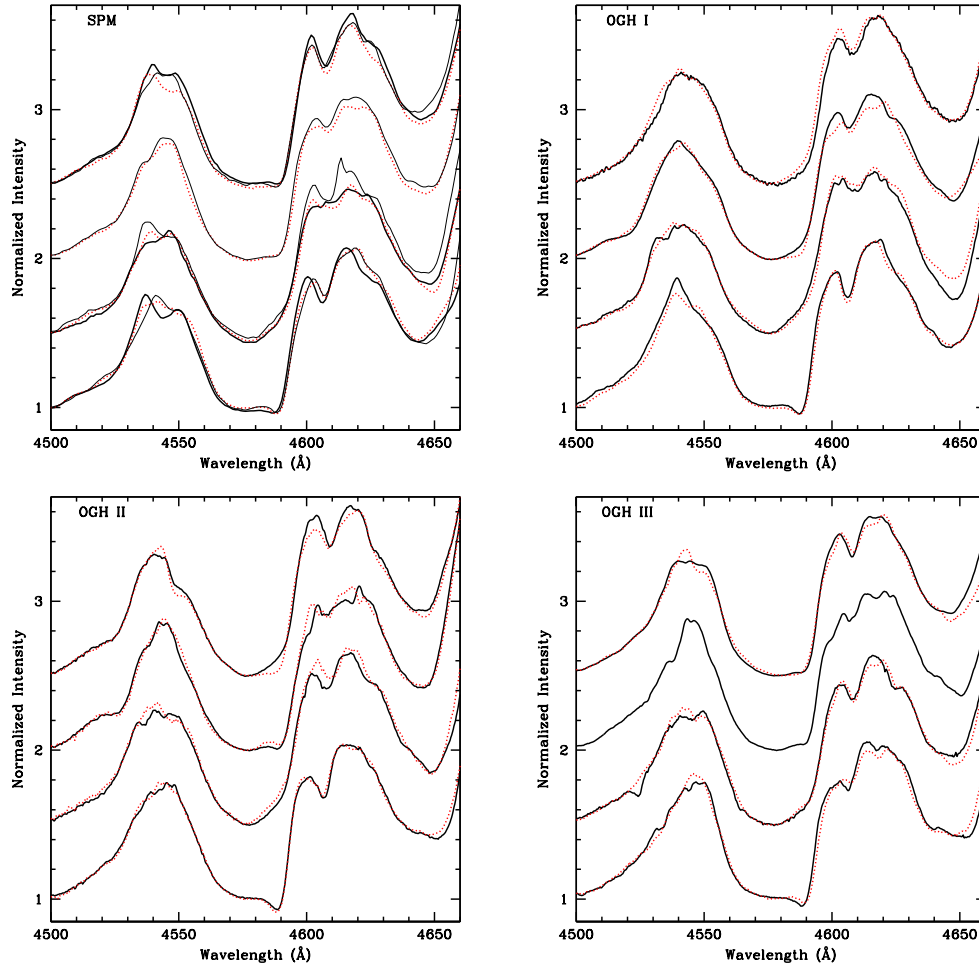


Fig. 3. Data from SPM (top left), OGH I (top right), OGH II (bottom left) and OGH III (bottom right) as in Figure 1 but here the spectra lying lowest in each plot are those in which N V 4604 has a *strong* P Cygni absorption component. Subsequent spectra stacked vertically correspond to the following nights of observation. Spectra of similar phases from contiguous cycles are superposed using different line types: the first cycle is plotted with thick lines, the second cycle with dots and the third cycle with thin lines. The *strong*-type profiles are always followed on the next night by an *absent*-type profile. The color figure can be viewed online.

of the spectra, and, for example, the changes seen in the OGH II spectra at phases 0.91 and 0.97 at 4585–4610 Å region lie in the range  $\sim 5\text{--}8\%$ . Given that  $S/N \sim 110n^{1/2}$  in these spectra and that each of the spectra is the average of  $n > 5$  individual exposures, most of these changes are well above what would be expected from random fluctuations.

#### 4. LINE FITTING PROCEDURE

The periodic line profile variations can be interpreted within three general scenarios. The first is one in which the intrinsic wind structure of the WR star changes over the 3.76 d period; in the second scenario, it is anisotropic, for example, having quadrants with different velocity gradients or ionization

fractions. In the third scenario, the inner portions of the wind have a stationary structure, but the outer regions do not, either because of some intrinsic instability or because of the perturbation from a companion. In this paper we focus on the first interpretation because it is the one that requires the smallest number of assumptions.

The line-profiles were modeled using the radiative transfer code described by Auer & Koenigsberger (1994). This is a simple code which computes the line profile produced in a wind having either a linear or a  $\beta$ -velocity law and an opacity distribution with arbitrary characteristics. The algorithm assumes spherical symmetry and uses the

TABLE 4  
DESCRIPTION OF INPUT PARAMETERS FOR LINE FITS<sup>a</sup>

Parameter	Value	Description
$R_{\max}$	4.2	Maximum extent of line-forming region, in units of $R_*$
$V_{\max}$	–	Terminal wind speed, in units of $V_{\text{th}}$
$V_{\text{th}}$	50	Thermal velocity, in $\text{km s}^{-1}$
$R_a$	3.9	Extent of linear acceleration region, in units of $R_*$
$R_i$	–	Radius of the $i$ -th region
$X_0$	–	Opacity parameter at $R_*$
$X_i$	–	Opacity parameter at $R_i$

<sup>a</sup>In Column 2 we list the values of those parameters that were held constant.

Sobolev approximation only in those portions of the wind where the approximation is valid. Where the Sobolev approximation breaks down (i.e., where the wind velocity gradient is small compared to the local Doppler velocities) it computes the radiative transfer precisely. A description of the input parameters is given in Table 4. The line is assumed to arise in a region whose maximum extent is  $R_{\max}$ . In the linear approximation,  $R_a$  is the distance over which the velocity increases; and  $R_i$ , with  $i = 1, 2, \dots, n$  are the radii of regions within the wind having different opacities. All distances are given in units of the stellar radius,  $R_*$ , which is the hydrostatic radius. The opacity in the different regions is parametrized with the opacity factor,  $X$ , which is a nondimensional parameter that enters into the line-profile calculation through the optical depth,  $\tau$ , defined as

$$\tau = \int \frac{X(r)}{[v(r)/v_{\text{th}}](r/R_*)^2} \varphi[x - v_z(z)] d(z/R_*), \quad (1)$$

where  $v(r)$  is the wind velocity law,  $v_{\text{th}}$  is the Doppler velocity,  $v_z$  is the projection of the wind velocity along the line of sight from the star to the observer in Doppler units,  $\varphi$  is the line profile function,  $x$  is the non-dimensional line frequency, and  $z$  is the coordinate along the line of sight. The maximum speed attained in the line-forming region is  $V_{\max}$ . It is specified in the code in units of  $v_{\text{th}}$ .

The code allows the value of  $X(r)$  to be specified for an arbitrary number of radial positions within the line-forming region. We represent its different values as  $X_i$  for the corresponding regions  $R_i$ . Note that by defining wind regions  $R_i$  with different  $X_i$  values, we are assuming that the excitation and/or ionization structure can change with distance from the stellar core.

Our analysis will be restricted to the “blue” wing of the N V 4604 line because its P Cygni absorption

component is formed in the column of wind material that lies along the line of sight from the observer to the continuum emitting core. Hence, it describes the behavior of wind material whose location is constrained, thus simplifying the interpretation. In addition, it is not contaminated by other lines. This is unlike its centrally-located emission which is blended with the P Cygni absorption produced by the neighboring N V 4620 Å doublet member.

We used a linear velocity law of the form  $v(r) = v_0 r$  because a standard  $\beta$ -velocity law failed completely to describe the observed line profiles. A  $\beta$ -law predicts a strong and sharp P Cygni absorption at the wind terminal speed ( $\sim 1900 \text{ km s}^{-1}$ ) which is not observed. This problem can be avoided if the line opacity goes to zero in the region where the wind velocity tends asymptotically to  $v_\infty$ . Hence, we opted to use a velocity law in which the wind accelerates linearly up to  $R_a$ , and then expands at a constant speed thereafter. The form of the velocity law in the code is  $v(r) = V_{\max} r/R_a$ , so the velocity at the stellar surface is  $v(R_*) = V_{\max}/R_a$ .

We chose to fix the value of  $R_{\max} = 4.2$  based on the deduced ionization structure of HD 50896’s wind from Hillier (1988; Figure 2) which shows that this is the extent of the region where the abundance of NV dominates over that of N IV. We also fixed  $v_{\text{th}} = 50 \text{ km s}^{-1}$ . This value was chosen in part because the ionization potential of NV is 98 eV which, under equilibrium conditions, corresponds to a thermal speed of  $37 \text{ km s}^{-1}$ , and in part because the code does not include turbulent broadening in the calculation and the added velocity serves to increase the Sobolev length accordingly. Since the velocities are given in units of  $v_{\text{th}}$ , the product  $V_{\max} v_{\text{th}} = v_\infty$  is constrained by the observations. We also fixed the value of the acceleration radius,  $R_a = 3.9 R_*$ .

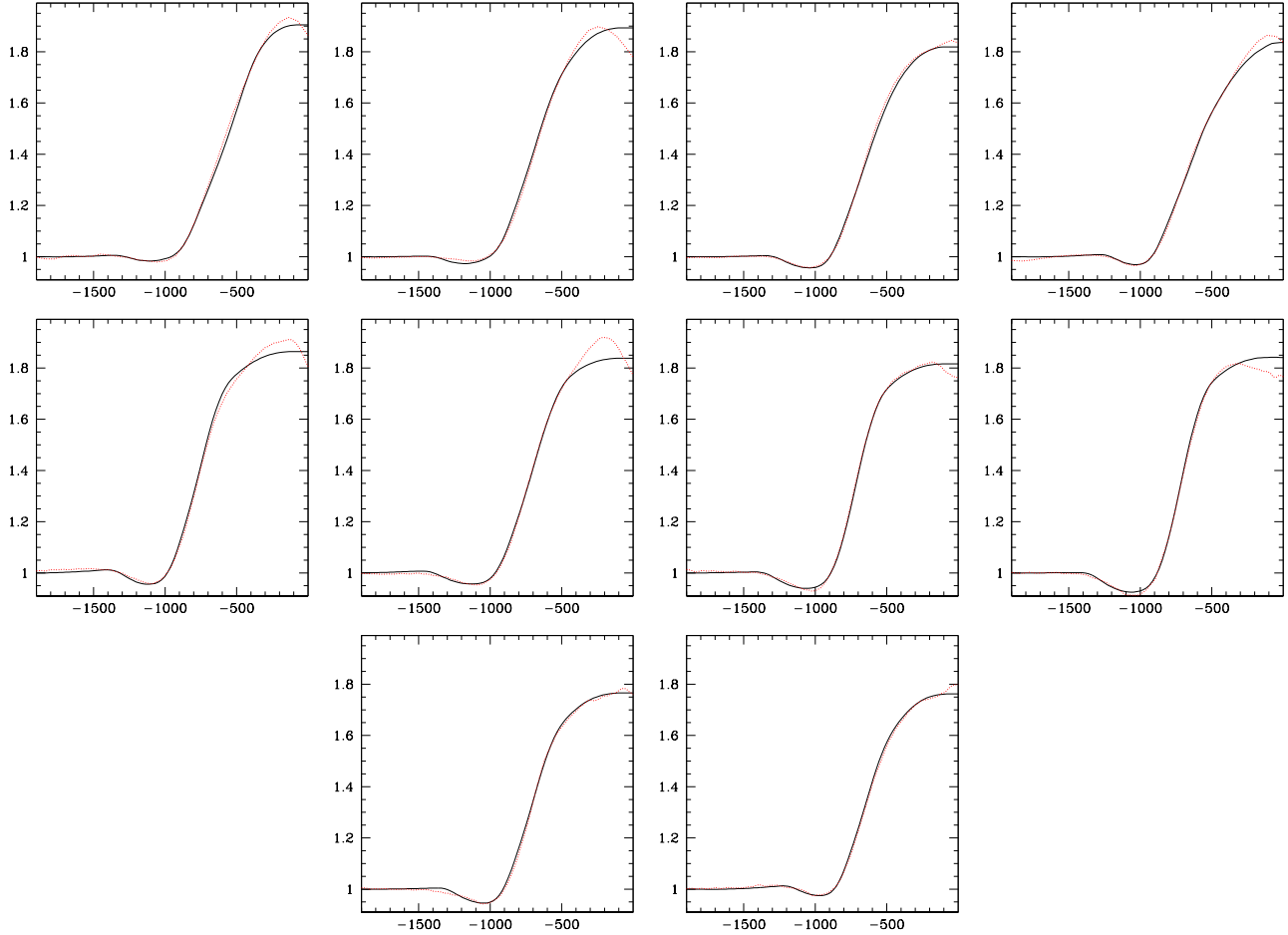


Fig. 4. Comparison of model calculations of the N V 4604 blue wing with the observations (dots) for the *strong* profiles. From left to right and from top to bottom: a, b, f, j, b27, b31, n22, n26, d03, d07. The abscissa is velocity in  $\text{km s}^{-1}$  with respect to the rest wavelength of N V 4604, the ordinate is normalized intensity. The color figure can be viewed online.

Values smaller than this lead to a sharp, blueshifted absorption component originating in the wind region that is moving at  $V_\infty$ , and these absorptions are not present in the observations.

It is important to note that, with the above parameters fixed, there are different combinations of  $V_{\text{max}}$ ,  $X_i$  and  $R_i$  which lead to very similar model line profiles. Thus, the line fits of Figures 4–6 are not unique. However, once  $v_{\text{th}}$  is specified,  $V_{\text{max}}$  is constrained to values that are consistent with  $V_\infty$ . Once  $V_{\text{max}}$  is fixed, the blue wing of the line profile is extremely sensitive to the values of  $X_2$ ,  $X_3$ ,  $R_2$ , and  $R_3$  and we are unable to find different combinations of these parameters which yield the same line-profile.

The detailed shape of the P Cygni profile depends strongly on the velocity gradient and on the opacity within the accelerating region. After numerous ex-

periments, we found it necessary to define at least three sub-regions within the accelerating region of the wind, each having different opacities. Keeping  $R_{\text{max}} = 4.2 R_*$ ,  $R_a = 3.9 R_*$  and  $v_{\text{th}} = 50 \text{ km s}^{-1}$  constant, we fitted each line individually in an iterative manner by varying only the values of  $X_i$ ,  $R_i$  and  $V_{\text{max}}$ . As noted above,  $V_{\text{max}}$  is limited by the terminal wind speed, so the range of values over which it can be varied is not very broad. However, it is important to note that a small variation in  $V_{\text{max}}$  modifies the velocity gradient and, hence, the Sobolev optical depth. Thus, variations in  $V_{\text{max}}$  that are within the uncertainties of the measured  $V_\infty$  lead to noticeable differences in the line profiles.

In general, a good fit was achieved after  $\sim 30$  iterations. A second pass on the entire set of profiles, with  $\sim 10$ – $20$  iterations each, yielded model profiles that differed from the observations within the noise

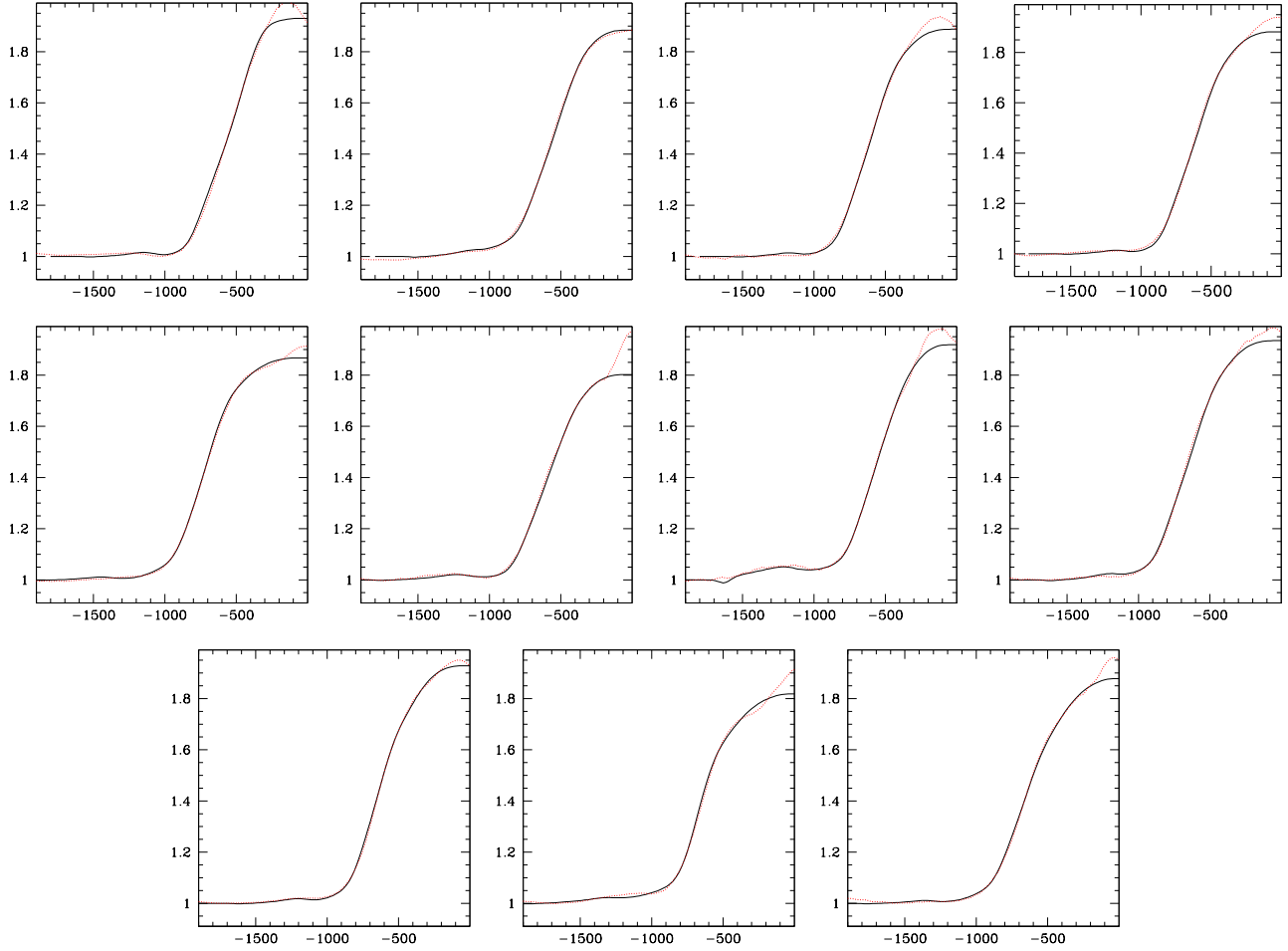


Fig. 5. Same as previous figure for the *weak* profiles. From left to right and top to bottom: e, h, i, l, b2, n20, n24, n25, d02, d05, d06. The color figure can be viewed online.

levels. The results are illustrated in Figures 4, 5, 6, where we grouped the profiles according to whether the P Cygni absorption is strong, weak or absent, respectively. In all cases, the fit to the blue wing, including the P Cyg absorption is excellent. We did not attempt to fit the centrally-located emission because it has contributions from the neighboring N V 4620, and it would be necessary to model the line transfer in the doublet. Thus, the model does not generally fit the observations around the emission maximum<sup>7</sup>.

We examined the uncertainty in the model fits by determining the change in the input parameters needed to produce a difference of 3% in the profile

<sup>7</sup>It is interesting to note, however, that the model generally under-predicts the emission intensity, consistent with the fact that the contribution from the N V 4620 emission will add on to the  $\lambda 4604$  emission and approach the value of the observed intensity.

with respect to the best fit model. In Figure 7 we plot the best-fit model for spectrum *n22* and the results obtained by changing the  $V_{\max}$ ,  $X_i$  and  $R_i$  input parameters one at a time. The range in these parameters is  $V_{\max}^0 \pm 1.2$ ,  $X_i^0 \pm 10$ , and  $R_i^0 \pm 0.05$ , where the 0-superindex indicates the best-fit values.

The optical depth along any ray depends on both the projected velocity gradient and the opacity at each particular line-of-sight velocity component. Hence, it is *a priori* difficult to determine the effects of modifying each of the free parameters of the calculation. Within the parameter space listed in Table 4, only a few guiding rules were found during the line-fitting process. For example, the slope of the line profile within the velocity range  $-800$  to  $-200$  km s<sup>-1</sup> is strongly influenced by the choice of  $R_2$ . The location and strength of the P Cygni absorption component is determined to a large extent by the values of  $V_{\max}$ ,  $X_3$  and  $R_3$ . Increasing the

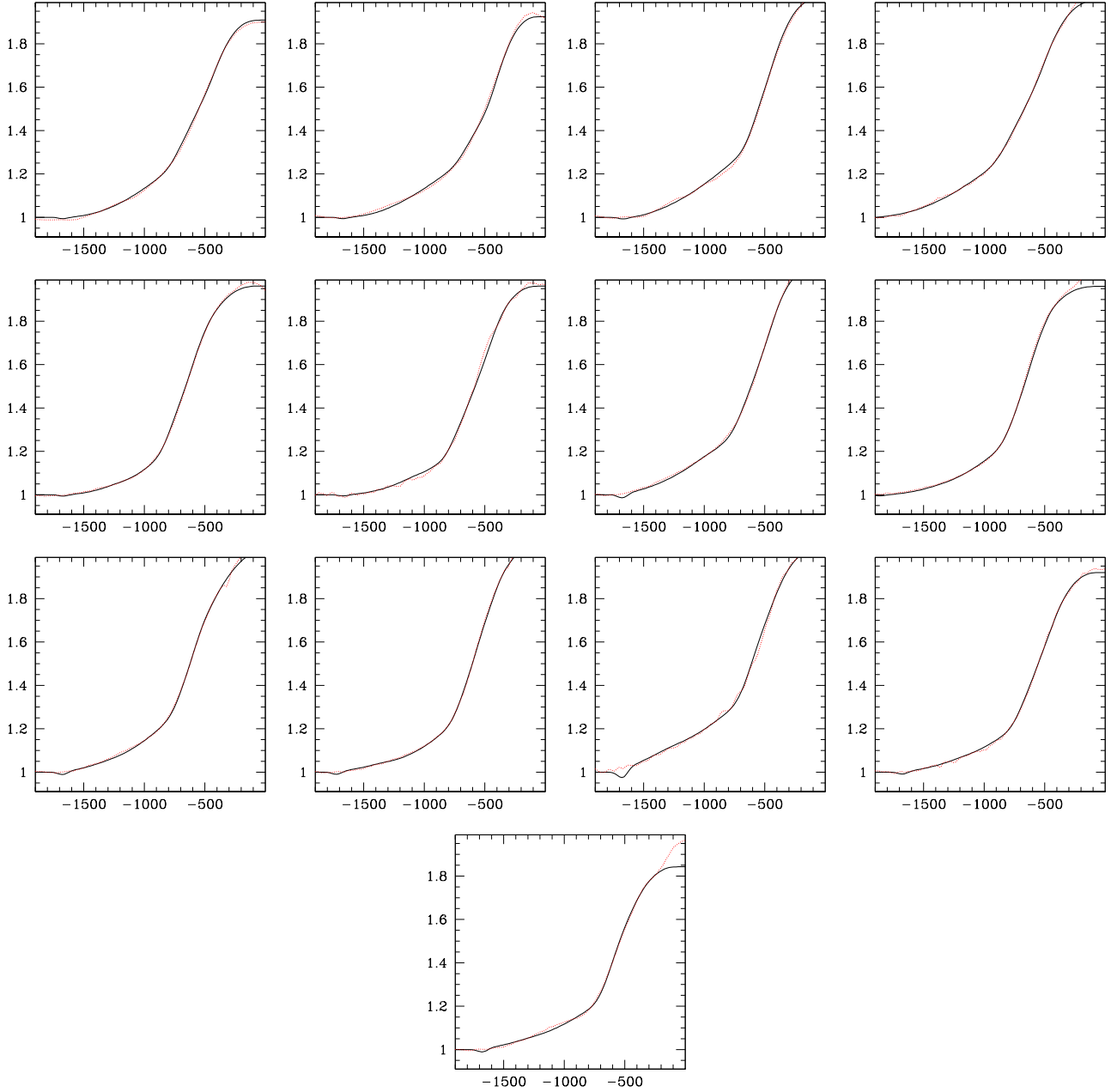


Fig. 6. Same as the previous figure for the *absent* profiles. From left to right and from top to bottom: c, g, k, b24, b25, b26, b28, b30, n19, n21, n23, d04, d08. The color figure can be viewed online.

value of  $X_3$  and  $X_4$  leads to an overall increase in the line strength. Changing the value of  $R_1$  affects the strength of the emission component at small line-of-sight velocities. The values of  $X_0$  and  $X_1$  need to be smaller than that of  $X_3$  to keep the line from being too strong at small velocities.

The input parameters that yielded the best fit to the P Cygni absorption of each spectrum are listed in Tables 1 and 2. The four regions into which the

wind was divided are identified by their maximum extent,  $R_i$ ,  $i = 1, \dots, 4$ . The results of the fits provide the values of  $R_i$  and their corresponding  $X_i$  values. The first region extends from  $R_*$  to  $R_1$ , where  $0.30 \leq R_1/R_{\max} \leq 0.35$ . The second region extends to  $R_2$ , where  $0.43 \leq R_2/R_{\max} \leq 0.52$ . The third region extends to  $R_3$ , where  $0.57 \leq R_3/R_{\max} \leq 0.74$ . The fourth region extends to  $R_{\max}$  and includes the portion of the wind that expands at a constant speed.

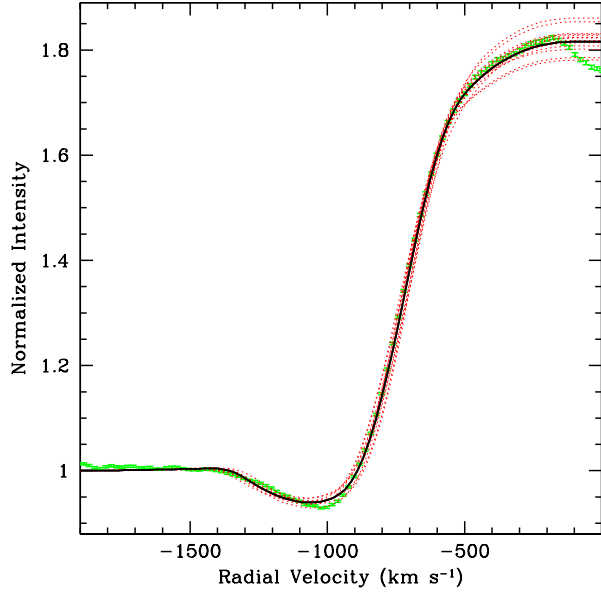


Fig. 7. Effects of changing the input parameters, one by one, on the shape of the line profile. The thick continuous line is the best-fit model. Dotted lines are the models with a different value for one of the following input parameters:  $V_{\max}$ ,  $X_1$ ,  $X_2$ ,  $X_3$ ,  $R_1$ ,  $R_2$ ,  $R_3$ . The observed spectrum (n22) is plotted as individual (green) points with error bars corresponding to  $S/N \sim 490$ . The “dip” in the observed line profile at  $\sim 0 \text{ km s}^{-1}$  is the P Cyg absorption component of the neighboring N V 4620 Å line. The color figure can be viewed online.

5. WIND STRUCTURE

Figure 8 shows the plot of the opacity parameter values,  $X_i$ , and the corresponding radial extent,  $R_i$ , derived from the line fits. The different symbols correspond to the three types of line profiles, *strong*, *weak* and *absent*, which henceforth will be referred to as *s*, *w* and *a*. The first noteworthy feature of this plot is that the opacity is, in general, small within the region closest to the star,  $\sim 1.5 R_*$ . This is consistent with the  $NV/NVI \ll 1$  abundance ratio in the innermost wind region (Hillier 1988; Figure 2). The opacity then rises significantly in  $R_2$ , and then declines again in  $R_3$  and  $R_4$ . Thus, the dominant opacity involved in the formation of the N V 4604 line is that of the wind material located in the  $R_2$  region, but with the *a* profiles having a significant contribution from material in  $R_3$ . The second feature is the marked difference in the behavior of the opacity factor in the *a* profiles from that of the *s/w* profiles. The former have smaller values of  $X_2$  and larger values of  $X_3$  than the latter.

Given that similar profiles may be obtained with different combinations of  $V_{\max}$ ,  $X_i$  and  $R_i$ , a second

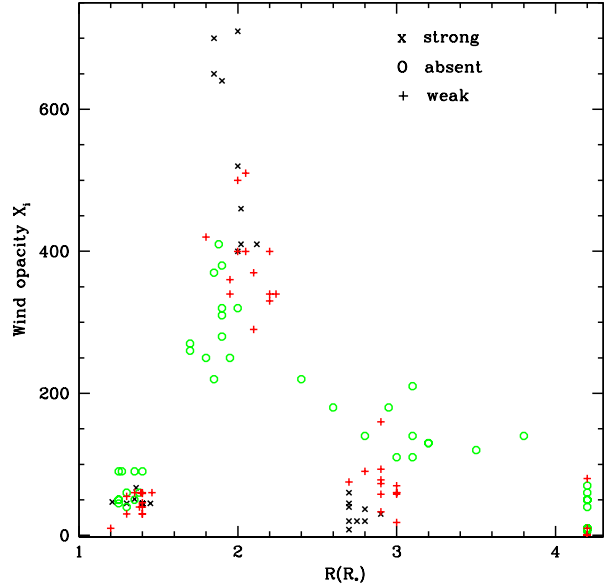


Fig. 8. Opacity parameter values ( $X_i$ ,  $i = 1, 2, 3, 4$ ) and their corresponding wind regions ( $R_i$ ) derived from the line-profile fits. The different symbols indicate the different types of profiles: cross (*s*), plus sign (*w*) and circle (*a*). The color figure can be viewed online.

set of model fits was computed with  $V_{\max} = \text{const} = 40$ , in order to illustrate the impact on the results. The fits were performed for the *s* and *a* profiles, since the *w* profiles are intermediate between these two. Figure 9 illustrates the difference between the results obtained above leaving  $V_{\max}$  as a parameter to be fit (left) and holding  $V_{\max}$  constant (right). The clear separation of the  $X_i$ ,  $i = 1, 2$  values for the *s* and *a* profiles persists as does the trend for a larger average value of  $R_3$  in the *a* profiles.

We now examine the 3.76 d phase dependence of the model fit parameters. In Table 3 we listed the night-to-night sequence of profile types for each epoch of observations. Table 5 shows the same description as Table 3, but the letters *s*, *a*, *w* are here listed in sets of four, corresponding to four consecutive nights of observation (Columns 2–5). In this representation it is evident that for each epoch the profile shape cycles through the type *s* (day 1), *a* (day 2) and *w/a* (days 3 and 4), where *w/a* means either a *w* or an *a* type. Columns 6–10 and 11–14 of Table 5 list the corresponding values of the opacity parameters  $X_2$  and  $X_3$ , respectively, in the same representation of sets of four nights. For each epoch, the column corresponding to the *s* profiles has the largest  $X_2$  value and smallest  $X_3$  value. This table clearly shows the 3.76 d cyclical pattern for

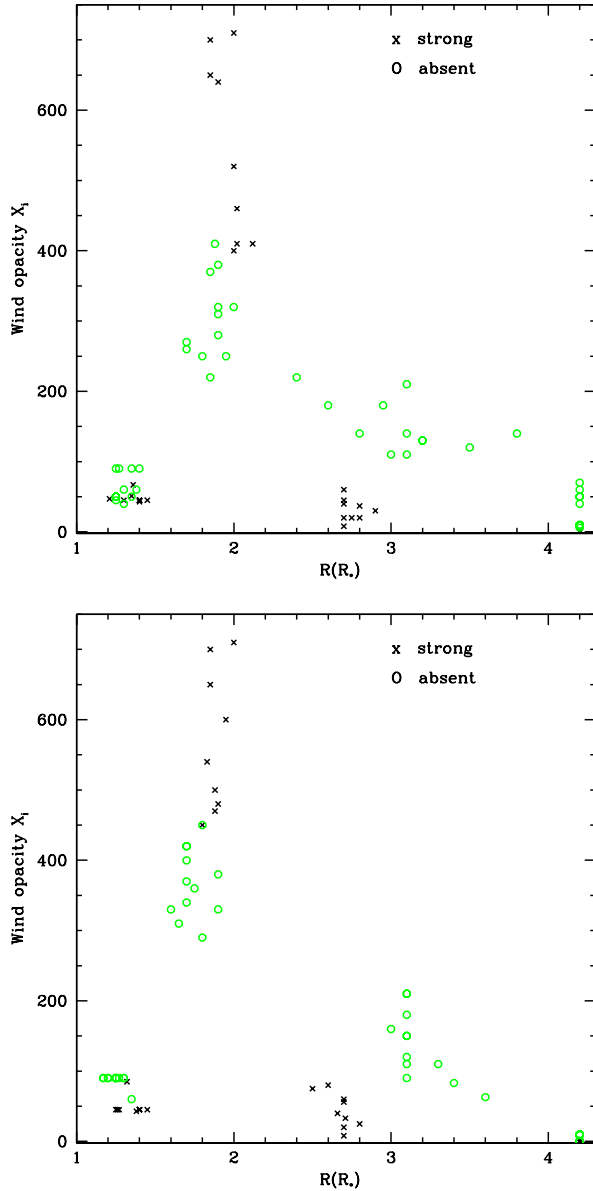


Fig. 9. Top: Same as previous figure, but showing only the values for the  $s$  and  $a$  profiles. Bottom: the same information, but this time from the model runs in which  $V_{\max}$  was held constant and the fits were performed for only the  $X_i$  and  $R_i$  values. The color figure can be viewed online.

each epoch, which is also illustrated in Figure 10. Phases were all computed with the same ephemeris from Georgiev et al. (1999). This figure also shows that the phases of maximum  $X_2$  and the amplitude of the variations differ from epoch to epoch. There is no significant difference in this figure if we plot the results obtained from the fits where  $V_{\max}$  was held constant.

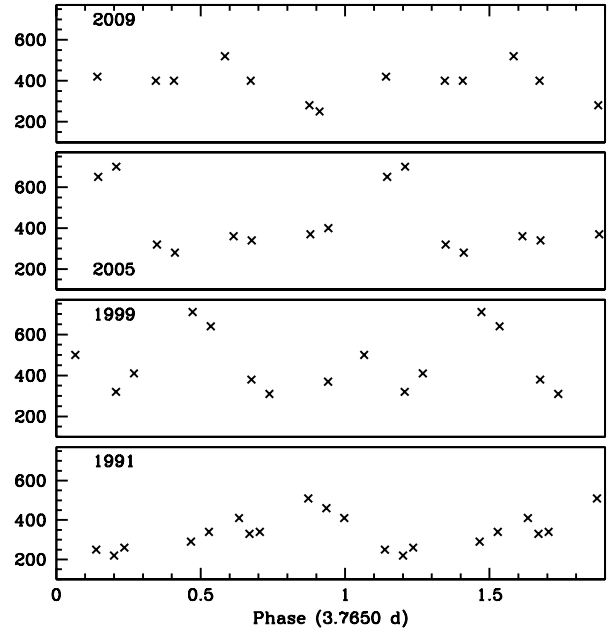


Fig. 10. Opacity parameter  $X_2$  from the line-fits plotted as a function of 3.7650 d phase for each of the 4 observation epochs. A modulation is present in each epoch, but it is not coherent from one epoch to the next. Same data are plotted twice.

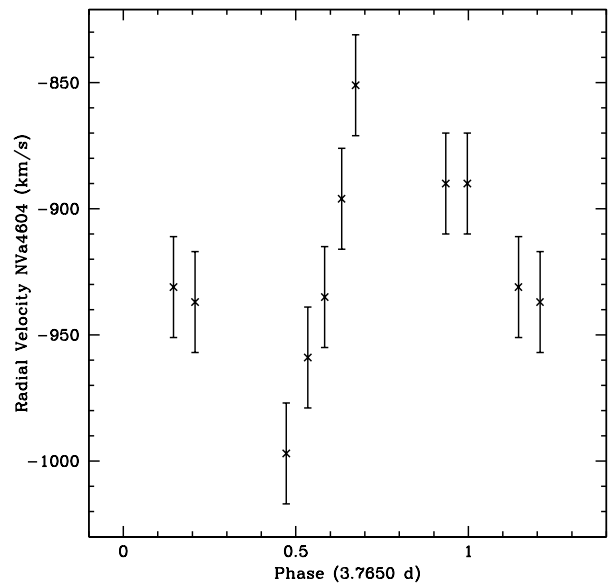


Fig. 11. Radial velocity variations of the N V 4604 P Cygni absorption component in the *strong* profiles plotted as a function of the 3.7650 d phase. A coherent variation over the 18 years of observations covered by these spectra is present.

TABLE 5  
PROFILE TYPES IN GROUPS OF FOUR<sup>a</sup>

Epoch	Type	$X_2$				$X_3$			
1991	s a - w	510	250	-	330	18	130	-	58
	s a w w	460	220	290	340	20	130	78	58
	s a w -	390	260	340	-	37	120	60	-
1999	- a a a	-	380	370	320	-	210	160	180
	s a - a	710	310	-	410	60	220	-	180
	s - w -	640	-	500	-	40	-	70	-
2005	- a w a	-	320	360	370	-	140	75	110
	s a w w	650	270	360	400	20	140	33	93
	s - - -	700	-	-	-	8	-	-	-
2009	- - - w	-	-	-	400	-	-	-	73
	s a w w	520	280	420	400	20	140	90	60
	s a - -	400	250	-	-	45	110	-	-

<sup>a</sup>Columns 2–5: Same information as given in Table 3 but here organized in sets of four sequential nights per row. For all epochs there is a sequence: *s* (day 1) → *a* (day 2) → *w/a* (days 3 and 4). Second block of 4 columns: opacity parameter  $X_2$  from the line fits; third block of 4 columns: opacity parameter  $X_3$ .

Given the above results we are led to conclude that the wind cycles through different opacity states over the 3.76 d period. These different states may be due to variations in the excitation/ionization structure or in the mass-loss rate, or a combination of the two. Such variations could be a consequence of pulsations in the underlying core. Piceno (2003) found periodic variation in the equivalent width of He II 4541 on timescales of 0.023 d, 0.044 d and 0.43 d on different nights of observation in the 1991 SPM data set, but not in the whole set of data, thus leaving an open question on the presence of possible non-radial pulsations. The precise mechanism by which the pulsations couple to the wind is still another open question (Townsend 2007).

An intriguing result concerns the radial velocity variations of the P Cygni absorption component of the *s* profiles. The centroid of these features was measured with a Gaussian fit from the location where the absorption meets the continuum level on the “blue” to the position of the emission component where the velocity is  $-500 \text{ km s}^{-1}$ . In Figure 11 the derived RVs from the nine *s*-type profiles obtained over the 18 years of observation are plotted as a function of the 3.76 d phase computed with the Georgiev et al. (1999) ephemeris. The error bars correspond to the measurement uncertainties, estimated to be  $\pm 30 \text{ km s}^{-1}$ . This figure shows a clear modulation. Thus, although the data points are too

few for a strong conclusion to be drawn, this result does suggest the presence of an underlying “clock” that retains coherence over very long timescales. It also indicates that it may be necessary to use only the *s* profiles to study the source of the “clock”.

## 6. DISCUSSION AND CONCLUSIONS

In this paper we used the N V 4604 line observed in HD 50896 spectra obtained over 18 years to explore the possible wind structure variations that may lead to the observed changes in the shape of this line. We find that the variability in the P Cygni absorption component can be explained in terms of changes in the opacity structure of the wind. Specifically, changes in the relative opacities in regions  $R_2 \sim 0.47 R_{\text{max}}$  and  $R_3 \sim 0.65 R_{\text{max}}$ , where  $R_{\text{max}}$  is the maximum extent of the N V 4604 line-forming region. Both these regions lie in the accelerating portion of the wind, according to the linear velocity law used to fit the profiles. The *strong* P Cygni absorptions are visible when the opacity in region  $R_2$  is larger than in  $R_3$ . When this ratio is inverted, the P Cygni absorptions vanish. Evidence of opacity enhancements has previously been found in other objects, such as the O7.5-star 68 Cyg (Prinja & Howarth 1988).

The temporal sequence for the appearance of the profiles is such that a profile with a strong P Cygni absorption is followed one night later by one in which

the absorption is absent. On the following two nights the profile may have either a weak or an absent absorption. On only one occasion (epoch 1991) there are *strong* profiles on two consecutive nights. Since the opacity depends on the mass-loss rate and on the ionization structure of the wind, its variation implies changes in these parameters.

The terminal velocity of HD 50896 is estimated at  $-1900 \text{ km s}^{-1}$  (Prinja, Barlow, & Howarth 1990; Howarth & Schmutz 1992). However, St-Louis et al. (1993) report that the most conspicuous absorption-line variability takes place between about  $-1800$  and  $-2800 \text{ km s}^{-1}$  for the major UV P Cygni lines. This implies that most of the variability occurs at speeds exceeding the normal maximum outflow velocity of the wind. The N V 4604 line does not provide information on these very large speeds, but it does tell us that the instability appears to be present at lower speeds as well. Given that UV lines arise from atomic transitions that are more optically thick, they are able to probe lower density regions of the wind. Such low density regions having high velocities are predicted to occur as a result of radiative instabilities (Owocki, Castor, & Rybicki 1988). Thus, the *absent* type N V 4604 profiles may occur when the radiative instabilities are more prevalent. We speculate that the *strong* type profiles might correspond to a more stable state of the wind, when fewer shocks are present. St-Louis et al. (1993) also concluded that the radiative instabilities probably play an important role in governing the line-profile variations that are observed in the UV.

One intriguing aspect of these perturbations is that significant changes in the line-profiles are observed on timescales of  $\sim 1$  day and no shorter. St-Louis et al. (1993) show how the UV P Cygni lines undergo changes on a day-to-day timescale. This is in contrast with, for example, the opacity enhancements mentioned above for 68 Cyg, where variations on timescales as short as 1 hr were observed (Prinja & Howarth 1988). Also relevant to this discussion is the presence of relatively narrow emission-like features (“sub-peaks”) superposed on the broad He II emission lines. Variable sub-peak structure in WR stars is generally associated with the presence of an inhomogeneous stellar wind. However, Drissen et al. (1989) concluded from their polarimetric data that the smaller-scale “blob” activity observed in other WRs is quite low in HD 50896. Hence, the variability of HD 50896 seems to originate in what might be described as organized episodes of unstable and stable states, rather than the random-like inhomogeneities that are present in many other WRs.

Also important to note is that at least one other WN-type star, WR1 (HD 4004) displays a variability similar to that of HD 50896 (Flores et al. 2007), so HD 50896 is not unique (see, also, St-Louis et al. (2009) for a discussion of variability in several other WR stars). Also, in the WN5 binary V444 Cygni, the N V 4603-21 doublet undergoes phase-dependent variations qualitatively similar to those of HD 50896. Specifically, the P Cygni absorptions are deepest during one orbital phase interval (primary eclipse), becoming weaker in the neighborhood of the secondary minimum, and disappearing completely at secondary eclipse (Münch 1950). This suggests that the weak P Cygni absorptions are indicative of a perturbed wind structure<sup>8</sup> which, in the case of V444 Cyg, probably results from a combination of irradiation and surface distortion due to tidal effects. In the case of HD 50896, the profiles with an absent P Cygni absorption are more prevalent than in V444 Cyg, indicating that the perturbation causing the absorption to vanish occurs more frequently.

The model we have applied to fit the line profiles is one based on the simplest set of assumptions; that is, we assume that the line profile variability is caused by variations in the wind properties, specifically, the opacity. Because we fit only the blue wing of the line profile, our conclusion applies, strictly speaking, primarily to the column of wind that is projected onto the continuum-emitting core. Hence, we are unable to distinguish between a cyclical (in time) variation of the entire wind structure and the variations that would be caused by different zones of the stellar wind (each with different properties) entering and leaving our line-of-sight due to stellar rotation.

Matthews et al. (1992) suggested a model consisting of two oppositely-directed jets, emerging at an angle with respect to the observer’s line-of-sight. They suggested that as the star rotates, the jets would alternately come into and out of the line-of-sight, thus producing the observed variability. Although the origin of such jets remains obscure, the general concept of a quadrupole-like wind structure may have a physical basis. Koenigsberger, Moreno, & Harrington (2010) proposed that the perturbations produced by the tidal forces in the eccentric binary system HD 5980 could lead to a variable wind structure as the system goes from periastron to apastron. Furthermore, since the tidal effects are stronger in the quadrant facing the companion than in the adjacent quadrants, the tidal perturbations

<sup>8</sup>The absent absorptions are attributed to the physical eclipse by Marchenko et al. (1997).

could, in principle, lead to a quadrupole-like wind distribution, independently of the eccentricity of the orbit. Demonstrating that a quadrupolar wind distribution in a rotating star reproduces the observed line-profile variations requires the use of a model that allows for departures from spherical symmetry.

In conclusion, we find that the N V 4604 line-profile variability may be understood in terms of a variable wind structure which involves changes in the N V opacity. The mechanism causing this variability remains to be determined.

GK acknowledges support from PA-PIIT/Universidad Nacional Autónoma de México grant and computing support from Ulises Amaya. AF acknowledges the sabbatical stay in the INAOE and support from Conacyt under the target financed project 121166 “Spectroscopy Variations of Wolf-Rayet Stars”, and by the UNACAR grant 1320.

#### REFERENCES

- Auer, L. H., & Koenigsberger, G. 1994, *ApJ*, 436, 859  
 Cherepashchuk, A. 1981, *MNRAS*, 194, 755  
 Crowther, P. 2007, *ARA&A*, 45, 177  
 Drissen, L., Robert, C., Lamontagne, R., Moffat, A. F. J., St-Louis, N., van Weeren, N., & van Genderen, A. M. 1989, *ApJ*, 343, 426  
 Firmani, C., Koenigsberger, G., Bisiacchi, G. F., Moffat, A. F. J., & Isserstedt, J. 1980, *ApJ*, 239, 607  
 Firmani, C., Koenigsberger, G., Bisiacchi, G. F., Ruiz, E., & Solar, A. 1979, in *IAU Symp. 83, Mass Loss and Evolution of O-Type Stars*, ed. P. S. Conti & C. W. H. de Loore (Dordrecht: Reidel), 421  
 Flores, A., Koenigsberger, G., Cardona, O., & de la Cruz, L. 2007, *AJ*, 133, 2859  
 Georgiev, L. N., Koenigsberger, G., Ivanov, M. M., St-Louis, N., & Cardona, O. 1999, *A&A*, 347, 583  
 Hillier, D. J. 1988, *ApJ*, 327, 822  
 Howarth, I. D., & Schmutz, W. 1992, *A&A*, 261, 503  
 Koenigsberger, G., Moreno, E., & Harrington, D. M. 2010, in *ASP Conf. Ser. 425, Hot and Cool: Bridging Gaps in Massive Star Evolution*, ed. C. Lietherer, P. Bennett, & J. van Loon (San Francisco: ASP), 209  
 Lamontagne, R., Moffat, A. F. J., & Lamarre, A. 1986, *AJ*, 91, 925  
 Marchenko, S. V., Moffat, A. F. J., Eenens, P. R. J., Cardona, O., Echevarría, J., & Hervieux, Y. 1997, *ApJ*, 485, 826  
 Matthews, J. M., St.-Louis, N., Moffat, A. F. J., Drissen, L., Koenigsberger, G., Cardona, O., & Niemela, V. S. 1992, in *ASP Conf. Ser. 22, Nonisotropic and Variable Outflows from Stars*, ed. L. Drissen, C. Leitherer, & A. Nota (San Francisco: ASP), 130  
 McLean, I. S. 1980, *ApJ*, 236, L149  
 Morel, T., St-Louis, N., Moffat, A. F. J., Cardona, O., Koenigsberger, G., & Hill, G. M. 1998, *ApJ*, 498, 413  
 Münch, G. 1950, *ApJ*, 112, 266  
 Owocki, S. P., Castor, J. I., & Rybicki, G. B. 1988, *ApJ*, 335, 914  
 Piceno, A. 2003, M. Sc. Thesis, INAOE, Puebla, Mexico  
 Prinja, R. K., Barlow, M. J., & Howarth, I. D. 1990, *ApJ*, 361, 607  
 Prinja, R. K., & Howarth, I. D. 1988, *MNRAS*, 233, 123  
 Skinner, S. L., Itoh, M., & Nagase, F. 1998, *New Astron.*, 3, 37  
 Skinner, S. L., Zhekov, S. A., Güdel, M., & Schmutz, W. 2002, *ApJ*, 579, 764  
 Stevens, I. R., & Willis, A. J. 1988, *MNRAS*, 234, 783  
 St-Louis, N., Chené, A.-N., Schnurr, O., & Nicol, M.-H. 2009, *ApJ*, 698, 1951  
 St-Louis, N., Howarth, I. D., Willis, A. J., Stickland, D. J., Smith, L. J., Conti, P. S., & Garmany, C. D. 1993, *A&A*, 267, 447  
 Townsend, R. 2007, in *AIP Conf. Proc. 948, Unsolved Problems in Stellar Physics*, ed. R. Stancliffe, G. Houdek, R. Martin, & C. Tout (Melville, NY: AIP), 345  
 van den Heuvel, E. P. J. 1976, in *IAU Symp. 73, Structure and Evolution of Close Binary Systems*, ed. P. Eggleton, S. Mitton, & J. Whelan (Dordrecht: Reidel), 35  
 van der Hucht, K. A., Conti, P. S., Lundstrom, I., & Stenholm, B. 1981, *Space Sci. Rev.*, 28, 227  
 Vázquez, G. 2003, M. Sc. Thesis, INAOE, Puebla, Mexico

O. Cardona: Instituto Nacional de Astrofísica Óptica y Electrónica, Luis Enrique Erro 1, Tonantzintla, Puebla, Mexico (ocardona@inaoep.mx).

L. de la Cruz and A. Flores: Facultad de Ingeniería, Universidad Autónoma del Carmen, Calle 56, 4. Cd. del Carmen, Campeche, Mexico (aflores, ldelacruz@pampano.unacar.mx).

G. Koenigsberger: Instituto de Ciencias Físicas, Universidad Nacional Autónoma de México, Ave. Universidad S/N, Col. Chamilpa, Cuernavaca 62210, Mexico (gloria@fis.unam.mx).